

Article

Constant Temperature Anemometer with Self-Calibration Closed Loop Circuit

Jamel Nebhen ^{1,*}, Khaled Alnowaiser ¹ and Sofiene Mansouri ²

¹ College of Computer Engineering and Sciences, Prince Sattam bin Abdulaziz University, Alkharj 11942, Saudi Arabia; k.alnowaiser@psau.edu.sa

² College of Applied Medical Sciences, Prince Sattam bin Abdulaziz University, Alkharj 11942, Saudi Arabia; s.mansouri@psau.edu.sa

* Correspondence: j.nebhen@psau.edu.sa

Received: 13 April 2020; Accepted: 12 May 2020; Published: 14 May 2020

Featured Application: Analysis of metrological velocity and temperature fields in gas flows in many areas of modern science and technology. Our Micro-Electro-Mechanical Systems (MEMS) calorimetric sensor is used in experimental studies in the field of fluid mechanics and thermodynamics, as well as in technical areas such as aerodynamics, aviation, automotive, climatology, ventilation and air conditioning, and refrigeration and heating.

Abstract: In this paper, a Micro-Electro-Mechanical Systems (MEMS) calorimetric sensor with its measurement electronics is designed, fabricated, and tested. The idea is to apply a configurable voltage to the sensitive resistor and measure the current flowing through the heating resistor using a current mirror controlled by an analog feedback loop. In order to cancel the offset and errors of the amplifier, the constant temperature anemometer (CTA) circuit is periodically calibrated. This technique improves the accuracy of the measurement and allows high sensitivity and high bandwidth frequency. The CTA circuit is implemented in a CMOS FD-SOI 65 nm technology. The supply voltage is 1.2 V while the core area is 0.266 mm². Experimental results demonstrate the feasibility of the MEMS calorimetric sensor for measuring airflow rate. The developed MEMS calorimetric sensor shows a maximum normalized sensitivity of 117 mV/(m/s)/mW with respect to the input heating power and a wide dynamic flow range of 0–26 m/s. The high sensitivity and wide dynamic range achieved by our MEMS flow sensor enable its deployment as a promising sensing node for direct wall shear stress measurement applications.

Keywords: MEMS calorimetric sensor; CTA circuit; amplifier; heating resistor; hot-wire anemometer

1. Introduction

Based on different measurement methods, micro-machined flow sensors can be divided into two groups, namely ‘direct’ measurement or ‘indirect’ measurement [1]. For direct measurement of wall shear stress, sensors usually use a floating element that is displaced laterally by the tangential viscous forces in the flow. This displacement implies a variation of an electrical parameter. For example, in [2] the authors developed a capacitive wall shear stress sensor with the floating element displacement implying a capacitive variation, reflected in an electric potential variation. A cantilever-based flow sensor using the piezoresistance effect is simulated in [3]. It has a low bandwidth. A capacitive airflow sensor based on out-of-plane cantilevers is designed and manufactured in [4]. These sensors present the clear advantage of a direct wall shear stress measurement. However, the necessary floating element implies an electro-mechanical coupling which is sensitive to vibrations. Moreover, all these calorimetric sensors suffer from their low bandwidth and low sensitivity. With miniaturization, the

mechanical resonance frequency comes close to the vibrations of the measured system structure. In the case of moving structures like vehicles vibrations affect at least the measure but can also affect the sensor integrity. For avoiding these drawbacks, indirect wall shear stress measurements were developed with various methods. For example, micro-fences using a cantilever structure and piezoresistors are presented in [5]. The exploitation of optical resonances such as whispering gallery modes of dielectric microspheres is proposed in [6]. The deflection of micro-pillars is presented in [7]. The physical principle used in thermal sensors consists of taking advantage of the convective heat transfer between an electrically heated resistor and a surrounding cooler fluid [1]. As they do not involve a mechanical moving part, thermal flow sensors are widely adopted when dealing with fluid dynamics including laminar or turbulent flows. Two main kinds of thermal sensors for velocity and wall shear stress have been developed: hot-wire and hot-film sensors. The difference between them lies in the designed structure: in hot-wire sensors the wire resistor is free from the substrate, fixed by two prongs and placed within the flow; on the other hand, the wire of hot-film sensors is deposited on a substrate and placed on a surface adjacent to the flow. Hot-wire sensors therefore enable heating uniformity and high sensitivity [8–10], but they are fragile and 3D thermal effects occur at the ends of the wire. They have also a low bandwidth because their cutoff frequency is very low. On the contrary, hot-film sensors are very robust despite their operational constraints. In particular, they suffer from heat losses through the substrate on which the wire is deposited. Various materials have thus been used to increase thermal insulation, such as silicon nitride [11], glass [12], or a flexible polymer [13–15]. These sensors, which are easy to flush-mount to the wall, are often used for detecting flow separation and for wall shear stress measurement. To improve the performance of hot-film sensors, the heat losses need to be reduced and bulk-machining techniques enable the deposition of the wire on a cavity-backed membrane [16].

In fluid mechanics, the flow rate is an intrinsic parameter of which derive several phenomena and principles. Therefore, measuring this quantity accurately and with high frequency is a challenge for researchers in this field [17–19]. To measure the flow velocity, a constant temperature anemometer is widely used. Indeed, it detects heat transfer between the hot element and the fluid. Convective heat transfer measurement is done by applying the closed loop and open loop method [20,21]. Turbulent flows are characterized by disordered movements of the particle fluid, with a fluctuation in speed and temperature. This phenomenon is very complex because it is governed by a nonlinear dynamic as well as by harmonics and sub-harmonics. However, its ability to measure the speed of fluids in turbulent flows and very narrow spaces is a significant advantage. In theory, to measure the velocity of air in turbulent flows, the bandwidth of the anemometer must be much greater than the frequency of flow fluctuation [22]. After the first micromachined thermal flow sensor reported in 1974 [23], with the rapid development of microfabrication technology, a growing interest in the microthermal flow sensors has been emerged [24–29]. To date, complementary metal-oxide-semiconductor micro-electro-mechanical systems (CMOS MEMS) technologies are increasingly being used to fabricate thermal flow sensors [30–32]. All fabricated flow sensors suffer from their low bandwidth and low sensitivity. Although the research in CMOS MEMS or MEMS-based flow sensor has been extensively focused on a variety of topics, few of these sensors were designed and fabricated specifically for detecting flow separation and for wall shear stress measurement. Their bandwidth and sensitivity are still low. Several reported micro thermal flow sensors are still power-hungry devices (>10 mW) with limited flow range and limited bandwidth [23,33], which cannot fully meet the requirements of flow separation applications. There is a strong motivation to develop such a high-performance MEMS flow sensor that is cost-effective and offers high bandwidth and high sensitivity.

The goal of this work was to design a MEMS calorimetric sensor with a high bandwidth and highly sensitive, self-calibrated constant temperature hot-wire anemometer (CTA). The CTA circuit allows injecting a variable current at the hot wire to keep its temperature constant. It provides a better thermal inertia by keeping the temperature constant thus a better cut-off frequency as well as a better sensitivity over a wide speed range [34]. We propose a measurement technique based on the control of a loop to maintain a constant temperature on the heating resistor and a current mirror in series to measure the current. At any value of the flow speed, the power delivered to the hot wire is the

maximum available. The power efficiency can be greatly increased as the voltage drop in the current mirror can be kept much lower than the constant voltage drop across the sensing resistor. The described circuit can be used with several control loop arrangements such as constant voltage, thermal sigma-delta modulation, or pulse width modulation (PWM). The circuit allows establishing different voltage values for the configuration of the loop. In addition, offset errors affect the accuracy of the current measurement. Therefore, the circuit includes the technique of offset cancellation and calibration. The paper is organized as follows. Section 2 describes the MEMS calorimetric sensor design. Section 3 presents the theoretical analysis of the flow sensor. Section 4 describes the principle of the CTA circuit. A CMOS implementation and experimental results are given in Section 5. Conclusions are drawn in Section 6.

2. Calorimetric Sensor Design

The calorimetric sensor is shown in Figure 1. It was manufactured by using a surface micro-machining technique. Three parallel micro-wires depict the sensitive section. Micro-wires are free from the substrate. A silicon oxide micro-bridge mechanically supports the sensitive section over a cavity. The three parallel micro-wires are designed perpendicularly to the flow. For the sensitive section, heating and wall shear stress measurement are combined in the central wire. The right and the left wires use the principle of the calorimetric phenomena. As a result, they represent a well solution to detect the flow direction. Owing to the flow, the right wire and the left wire are cooled differently. Therefore, the upstream wire becomes cooler compared to the downstream wire. As a result, the flow direction is known by their temperature difference. Table 1 shows the geometric sizes of each wire. They measure 1-mm-long, 3- μm -wide and less than 0.5- μm -thick. The wires are isolated in a 20- μm deep cavity in order to increase their convective heat transfer and to avoid heat losses. Therefore, the wires are within the flow. A high temperature gradient is guaranteed by the high aspect ratio of the wires in the flow direction. A homogeneous temperature is ensured along the single wire. The mechanical robustness of the wires despite their length over the flow is guaranteed by their maintenance with periodic silicon oxide bridges.

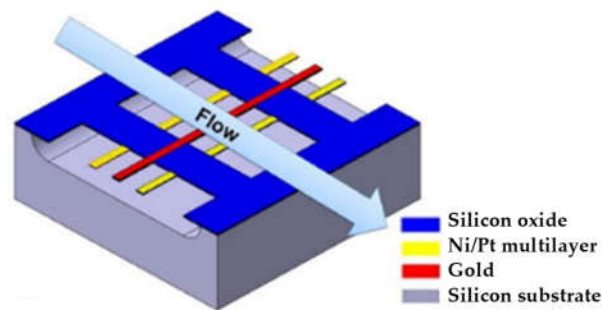


Figure 1. Overview of the calorimetric sensor design.

Table 1. Calorimetric sensor geometric sizes.

Size	Heater	Sensing Wires	Bridges
Width (μm)	3	3	7
Length (mm)	1	1	0.03
Thickness (nm)	200	120	450

Three layers depict the central wire, as shown in Figure 2. The first is an Au/Ti layer, which is the heater. This material was chosen because of its high temperature stability. The second is a Ni/Pt/Ni/Pt/Ni multilayer, which is the measurement wire. It reaches about 130-nm-height. We chose this material because of its high temperature-dependent resistivity. The last is a SiO_2 insulator layer to separate the first two layers. The external power supply attacks only the heater layer. Therefore, the heater layer heats the whole sensor. To improve the signal to noise ratio, heating and measure are electrically uncoupled. The 4-point measurement technique is used to measure the current. A current

of 100-μA crosses the measurement wires. Therefore, the resistances measurements are realized without heating the wires.

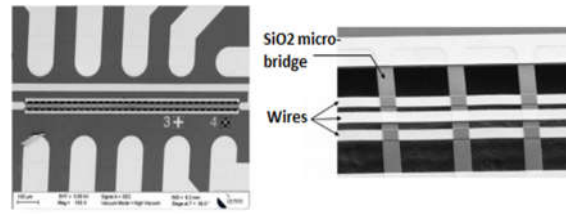


Figure 2. SEM microphotograph of the fabricated sensor with a magnified image of the sensitive section.

3. Theoretical Analysis of the CTA Circuit

A constant temperature anemometer is defined by its general differential equation. Therefore, the energy stored in a wire of length l and diameter d can be written as:

$$\frac{dQ_s}{dt} = \frac{dQ_e}{dt} - \frac{dQ_{fc}}{dt} \tag{1}$$

where Q_s is the energy stored in the hot wire, $Q_e = R_w I^2$ is the energy provided by the Joule effect and Q_{fc} is the energy transferred from the wire to the outside.

By injecting a current I , the wire is brought to a temperature higher than the fluid temperature. The main source of dissipation in the hot wire is the convection force where h is the heat transfer coefficient. It is related to the Nusselt number, which can be written as:

$$Nu = \frac{hd}{k_f} \tag{2}$$

where k_f is the thermal conductivity of the surrounding fluid. By replacing h by its expression as a function of the Nusselt number and by considering a wire of finite length l , the formula of the heat transfer by convection force can be written as:

$$Q_{fc} = \pi l k_f (T_w - T_0) Nu \tag{3}$$

The Nusselt number Nu expresses the efficiency of heat transfer by convection. The linear dependence between the resistance of the wire and its temperature can be written as:

$$R_w I^2 = \pi l k_f (T_w - T_0) Nu \tag{4}$$

where R_w is the operating resistance of the hot wire. The temperature variation of the CTA system can be written as:

$$T_w - T_0 = \frac{R_w - R_0}{\alpha_0 R_0} \tag{5}$$

where R_0 is the resistance of the wire at room temperature and α_0 is the temperature coefficient of the material used at room temperature. Adding Equations (4) and (5) we will have

$$R_w I^2 = \pi l k_f \left(\frac{R_w - R_0}{\alpha_0 R_0} \right) Nu \tag{6}$$

From [6], it is demonstrated that the Nusselt number Nu can be written as:

$$Nu = 0.42 Pr^{0.2} + 0.57 Pr^{0.33} Re^{0.5} \tag{7}$$

where Pr is the Prandtl number and Re is the Reynolds number. Using Equation (7) in Equation (6), the linear dependence between the resistance of the wire and its temperature can be written as:

$$\frac{R_w J^2}{(R_w - R_0)} = A + BV^{0.5} \tag{8}$$

with

$$A = 0.42 \frac{\pi k_f l}{\alpha_0 R_0} Pr^{0.2} \tag{9}$$

and

$$B = 0.57 \frac{\pi k_f l}{\alpha_0 R_0} Pr^{0.33} \left[\frac{\rho d}{\mu} \right]^{0.5} \tag{10}$$

where ρ is the density of the fluid, μ is the dynamic viscosity of the fluid and V is the average speed of the fluid.

Therefore, Equation (8) represents the fundamental relationship of the constant temperature hot-wire anemometer. The CTA circuit uses a regulation loop. It is composed of two opamps as shown in Figure 3. The first opamp has a time constant of $M1$ and the second opamp has a time constant of $M2$. Therefore, this technique allows having a second order system. As a result, the transfer function of the complete system can be written as:

$$H(s) = \frac{G}{1 + sM' + s^2M''} \tag{11}$$

where M' is the first order time constant of the differential equation of the control loop with $M' = M1 + M2$, M'' is the second order time constant of the differential equation of the control loop with $M'' = M1 \times M2$ and G is the total gain of the regulation loop. The third order time constant of the constant temperature hot-wire anemometer equation is an invariable intrinsic parameter which depends on the flow velocity, the superheat coefficient, and the time constant of the regulation loop [34]. This parameter defines the general cutoff frequency of the anemometer.

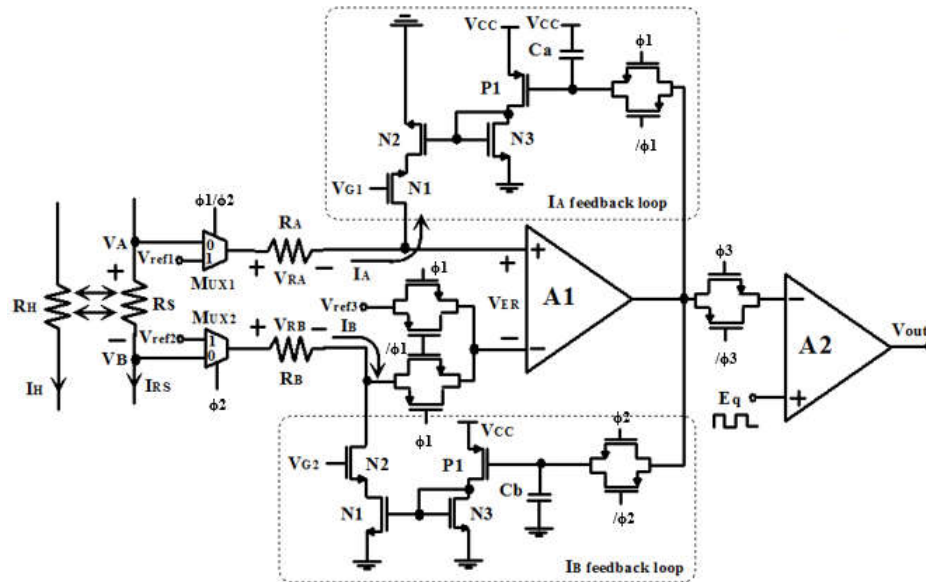


Figure 3. Circuit of the constant temperature anemometer (CTA).

The system response to a square wave has been analyzed [35]. To obtain a better cut-off frequency, the anemometer must be adjusted so as to have an index response with 15% overshoot. The cut-off frequency of the constant temperature hot wire anemometer can be written as:

$$f_{cut} = \frac{1}{1.3\tau_w} = \frac{1}{2\pi \left(\frac{M'M''}{G} \right)^{\frac{1}{3}}} \quad (12)$$

where τ_w the time from the start of the pulse until the signal reaches an amplitude of 3% compared to its maximum amplitude h . Finally, Freymuth demonstrated the following equation [8]

$$\frac{M''}{G} = \frac{M_1 M_2}{G_1 G_2} = \frac{1}{(2\pi)^2 \cdot GBWP_1 \cdot GBWP_2} \quad (13)$$

where G_1 is the closed loop gain of the first opamp in the regulation chain, G_2 is the closed loop gain of the second opamp in the regulation chain, $GBWP_1$ is the product gain bandwidth of the first opamp in the regulation chain and $GBWP_2$ is the product gain bandwidth of the second opamp in the regulation chain. Knowing that the equation of the cutoff frequency of the hot wire in the Wheatstone bridge can be written as:

$$f_w = \frac{1}{2\pi M} \quad (14)$$

Therefore, by combining Equations (12)–(14) we have the following equation

$$f_{cut} = (f_w \cdot GBWP_1 \cdot GBWP_2)^{\frac{1}{3}} \quad (15)$$

As a result, from Equation (15), if the cut-off frequency f_{cut} must be 100 times greater than the cut-off frequency f_w of the hot wire, then, the geometric mean $GBWP$ must be 10 times greater than the cut-off frequency f_{cut} of the anemometer. Therefore, from theoretical study we can calculate the gain of the first and the second opamp as well as the bandwidth of the MEMS calorimetric sensor.

4. Principle of the CTA Circuit

Figure 3 shows the main architecture of the CTA circuit. It has three modes of operation; two modes for calibration and offset correction, which are M1 and M2, and an M3 mode for normal operation. Normal mode, M3, represents the state of the CTA circuit when it detects and amplifies the error signal V_{ER} . This error signal represents the difference between the voltage drop V_{RS} created by the sensitive resistor R_S and the target voltage V_{TR} , $V_{ER} = V_{RS} - V_{TR}$. We have two terminals of the sensitive resistor R_S that are wired to nodes V_A and V_B . We have also two resistors R_A and R_B , which create down-level shifters, V_{RA} and V_{RB} , which allow separating of nodes V_A and V_B in order to provide a high-power heating. Finally, we have cascade current sources delivering bias currents I_A and I_B . To adjust currents I_A and I_B , we use linear feedback loops. Two analog multiplexers, MUX_1 and MUX_2 , are placed between resistors R_A and R_B in order to ensure different modes of operation. Moreover, they must withstand the voltages V_A and V_B . When V_{RS} across the sensitive resistor is equal to target V_{TR} , it must occur a zero differential voltage $V_{TR} = 0$ V across the amplifier in normal operating mode. Then, for a desired V_{TR} , we must correctly adjust the two-current sources in order to cause two-voltage drops, V_{RA} and V_{RB} , across resistors R_A and R_B , respectively.

The two calibration operation modes M1 and M2 allow defining the two currents I_A and I_B .

$$V_{TR} = I_A R_A - I_B R_B = V_{RA} - V_{RB} \quad (16)$$

In fact, three digital signals are used to control the two current sources feedback loops. They allow the control of the topology of the complete circuit. Moreover, they allow selecting the corresponding operation mode, as shown in Figure 4. The adjustment of the voltage drops V_{RA} and V_{RB} is ensured by three voltage references V_{ref1} , V_{ref2} , and V_{ref3} during the two calibration phases. A common-mode voltage appears at the input terminal of the operational amplifier during the calibration phase of the CTA circuit. The reference voltage V_{ref3} determines this voltage.

When $\{\phi_1, \phi_2, \phi_3\} = \{1, 0, 0\}$, the first mode M1 is active, as shown in Figure 4a. During this mode, the switching of the positive input of the operational amplifier to V_{ref1} and the connection of V_{ref3} to

the negative input allows the adjustment of the voltage V_{RA} . Therefore, during this mode, the positive feedback loop of the operational amplifier will be closed. We set V_{ref1} to the typical value of V_A . In the input range of the operational amplifier, we use V_{ref3} to cause a desired voltage drop V_{RA} .

$$V_{RA} = V_{ref1} - V_{ref3} \tag{17}$$

The setting of the voltage to the capacitor C_a ensures the adjustment of the current I_A by this closed loop. The value of this capacitor is set to maintain the voltage gate at the transistor P1 at the end of operation of this mode. Furthermore, this capacitor also allows defining of the dominant pole of the active feedback loop. Transistors P1 and N3 compose the current mirror. It allows to reverse the phase of this loop, which ensures good stability.

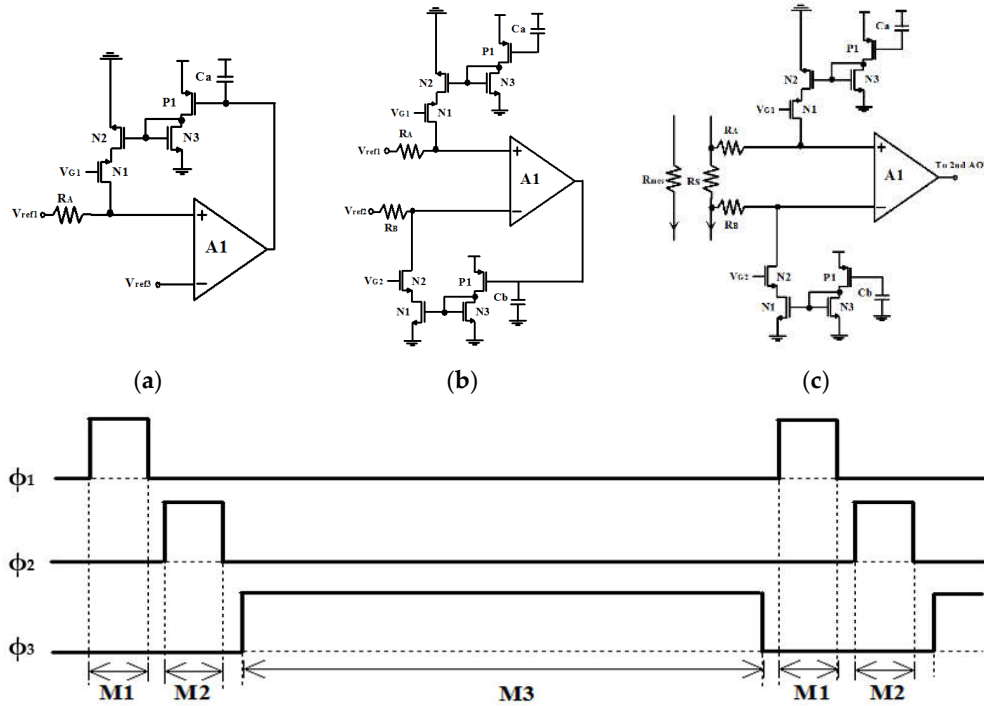


Figure 4. Equivalent circuits for the three operation modes M1, M2, and M3 ((a)–(c), respectively) with their selected digital signals ϕ_1 , ϕ_2 , and ϕ_3 .

The second mode, M2, is active when $\{\phi_1, \phi_2, \phi_3\} = \{0, 1, 0\}$, as shown in Figure 4b. In this case, the drop voltage V_{RB} is ensured by adjusting the current I_B of the CTA circuit. In this mode of operation, the voltage V_{ref1} is at the positive input terminal of our CTA circuit and the voltage V_{ref2} is at its negative input. When this mode ends, the drain current I_B must be maintained by adjusting the capacitor C_b on an appropriate voltage like in the first mode. In this mode, V_{ref2} must be greater than V_{ref3} .

$$V_{RB} = V_{ref2} - V_{ref3} \tag{18}$$

The last mode M3, called normal mode, is active when $\{\phi_1, \phi_2, \phi_3\} = \{0, 0, 1\}$, as shown in Figure 4c. In this case, we open the first and the second calibration loop. As a result, the sensitive resistor is directly connected to the input terminal of our CTA circuit. Therefore, the output voltage V_{out} of the CTA circuit can be written as

$$V_{out} = A_1 \cdot A_2 (V_A - V_{RA} - V_B + V_{RB}) = A_1 \cdot A_2 (V_{RS} - V_{TR}) = A_1 \cdot A_2 \cdot V_{ER} \tag{19}$$

where A1 and A2 are the amplifier's open loop gain. Figure 5 shows the complete circuit of the CTA sensor. In the feedback loop, we find the operational amplifier. It allows controlling of the current through the sensitive resistor. A stable voltage drop at V_{TR} is provided by this current. When

the M1 and M2 calibration modes are activated, the drain current through the sensitive resistor is maintained by the capacitor C_3 . The dominant pole in the circuit is defined by this capacitor C_3 . Furthermore, a current mirror composed of transistors N4 to N7 with an N:1 ratio allows detection of the current I_{RS} . This current mirror then generates a current I_{MES} .

$$V_{RS} = \frac{V_{TR}}{I_{RS}} = \frac{V_{TR}}{N \cdot I_{MES}} \quad (20)$$

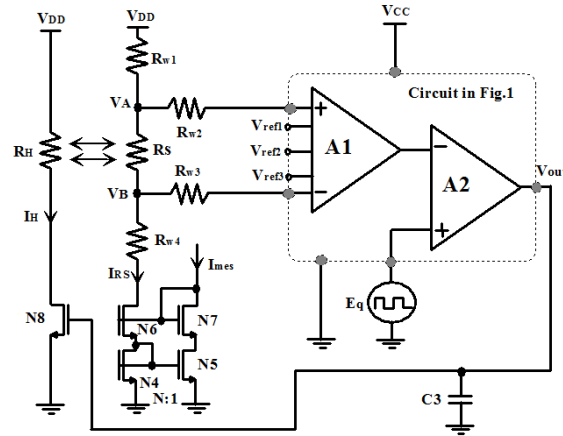


Figure 5. CTA circuit with R_{w1} , R_{w2} , R_{w3} and R_{w4} are the wire resistances.

5. Experimental Results

Prototypes of the CTA circuit were fabricated and experimentally characterized using CMOS FD-SOI 28-nm technology. The total chip area including pads was 0.266 mm². The die photograph of the CTA circuit is shown in Figure 6.

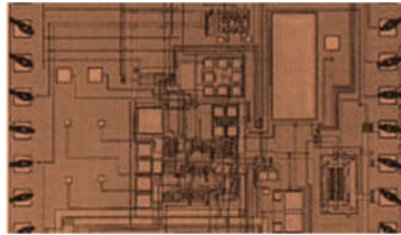


Figure 6. Chip microphotograph of the CTA circuit in CMOS FD-SOI 28-nm technology and 0.266-mm² area.

The supply voltage of the sensitive resistor is $V_{DD} = 3$ V and of the CTA circuit is $V_{CC} = 1.2$ V. A miller operational transconductance amplifier (OTA) was used with the resistors R_A and R_B equal to 1 k Ω to minimize the input thermal noise. Moreover, these resistors allowed reduction of energy consumption. Finally, resistors R_A and R_B also allowed the minimizing of errors introduced by the resistances of the connection wires of the CTA circuit, which were R_{w1} to R_{w4} . Capacitors values were chosen as $C_1 = C_2 = C_3 = 12$ pF. A ratio of $N = 20$ between the transistors N4/N6 and N5/N7 was set to reduce the power consumption. To test the CTA circuit, the nominal resistance of the sensitive resistor was 750 Ω at 0 $^{\circ}$ C. The measurement result when different target voltages $V_{TR} = \{0.5$ V, 1 V, 1.5 V, 2 V $\}$ were applied to the sensitive resistor with the digital signals ϕ_1 , ϕ_2 and ϕ_3 is shown in Figure 7. We set references $V_{ref1} = 3$ V, $V_{ref3} = 0.5$ V and we varied the reference $V_{ref2} = \{2.5$ V, 2 V, 1.5 V, 1 V $\}$. The curves show that the applied reference voltages were stable. In addition, after each calibration phase, there was a change in voltage V_{RS} . Figure 8 shows the transient response of the sensitive resistor for a voltage $V_{RS} = 2$ V. By setting the reference voltages $V_{ref1} = 3$ V, $V_{ref2} = 1$ V and $V_{ref3} = 0.5$ V, we can see that the increase in sensitive resistor temperature ensured a decrease in current flowing through the

heat resistor R_H . For this transient response, the steady state current reached the value I_{RH} of 3 mA and a sensitive resistor of 750Ω after 30 s.

To find the cut-off frequency of the CTA circuit, a 1-kHz frequency and 50-mV amplitude square wave signal was used to optimize its frequency response. This square wave signal was applied to the non-inverting input of the differential amplifier A1. Figure 9 shows the square wave response of the CTA circuit. The cut-off frequency at -3 dB of the CTA circuit is defined as $f_{cut} = 1/(1.3\tau)$ [8], where τ is the pulse width. Therefore, our CTA circuit has a cut-off frequency of 60 kHz.

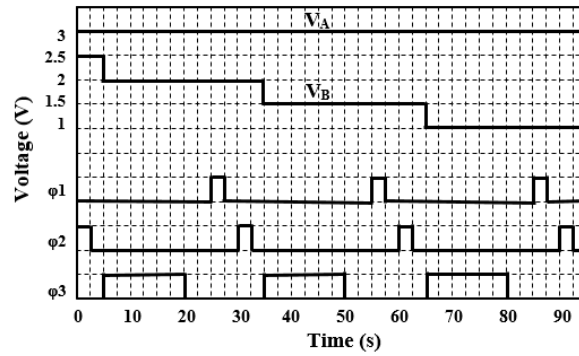


Figure 7. Measurement results for target voltage (V_{TR}) = {0.5 V, 1 V, 1.5 V, 2 V}.

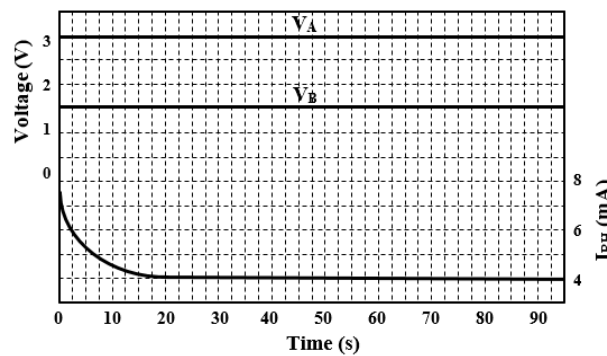


Figure 8. Transient response of the CTA circuit with $V_{TR} = 1.5 \text{ V}$.

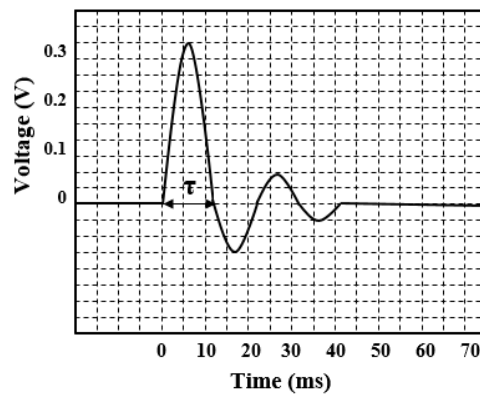


Figure 9. Square-wave time response of the CTA circuit.

The fabricated MEMS calorimetric sensor was packaged into a printed-circuit board (PCB). The PCB was polished with a chamfer to reduce the possible flow separation and make sure a stable boundary layer was generated. The packaged flow sensor was tested at the test-section of an open-loop suction type wind tunnel (LW-8233, LonGwin, Taiwan), which was attached to a gantry as shown in Figure 10. The wind tunnel has a pitot tube (DP-Calc 8710, TSI, MN, USA) based reference

flow meter for the free stream airflow measurement. With the heater resistor R_H working on the temperature of 40 K, the measured power consumption P of R_H under the input airflow of 0–26 m/s was 3–3.5 mW. More power was needed to maintain a constant overheated temperature due to the cooling effect of fluids flow. Accordingly, the required heater current I_H was increased with the enhanced joule heating. The measurement of the MEMS calorimetric sensor was performed with an input airflow from 0 m/s to 26 m/s. The calorimetric sensor had a high sensitivity S of 0.35 V/(m/s) at the linear low velocity region. Herein, the sensitivity of the MEMS calorimetric sensor is defined as the slope of the linear fit between two calibrated data points.

Table 2 shows the comparison between our MEMS calorimetric sensor and the other reported CMOS thermal flow sensors. Our MEMS calorimetric sensor gains a prominent normalized sensitivity S of 117 mV/(m/s)/mW with respect to the input heating power, which shows a $21 \times$ higher sensitivity as compared to others work [9,36–40]. The calorimetric sensor in [41] has a high sensitivity of 103 mV/(m/s)/mW. Compared to the sensor of [41], our MEMS calorimetric sensor reaches a higher sensitivity, higher bandwidth, and lower silicon area. Moreover, our measured MEMS calorimetric sensor has a higher bandwidth of 60 kHz compared to all other reported thermal flow sensors. Therefore, our MEMS calorimetric sensor, with the merits of a robust design, high sensitivity, low silicon area, and wide dynamic range, can be deployed as a promising sensing node for direct wall shear stress measurement.

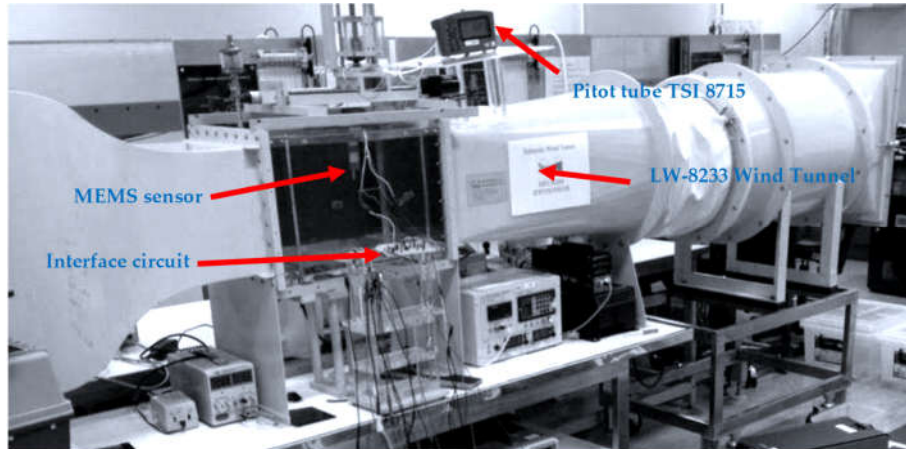


Figure 10. Experimental setup for the micro-electro-mechanical systems (MEMS) calorimetric sensor testing in the wind tunnel with the reference flow velocity read by Pitot tube.

Table 2. Comparison between the reported calorimetric flow sensor and current work.

Reference	Die Size, mm ²	Fluid	Flow Range, m/s	Power, mW	Sensitivity S , mV/(m/s)/mW	Bandwidth, kHz
[36]	12	Air	0~26	9.4	0.936	N/A
[37]	14	N ₂	-26~26	12.1~17.7	5.56	10
[9]	11.7	N ₂	-26~26	12.2~16.7	0.0582	12
[38]	N/A	N ₂	0~85	13	4.24	48
[39]	16	N ₂	-3.33~3.33	4	2.3	32
[10]	36	Air	0.5~40	2~452.6	3.93	21
[41]	3.24	Air	0~19.4	3.26~3.83	103	52
This work	0.266	Air	0~26	3	117	60

6. Conclusions

This paper presented an MEMS calorimetric sensor designed for bidirectional wall shear stress measurement, and aiming flow separation detection for flow control applications. We successfully designed and fabricated a MEMS calorimetric sensor by using a CMOS FD-SOI 28 nm technology. The supply voltage is 1.2 V while the core area is 0.266 mm². A detailed investigation of MEMS calorimetric sensors' sensitivity, bandwidth, power consumption, and flow range was performed with wind tunnel testing. Test results showed that our MEMS calorimetric sensor achieves a

maximum normalized sensitivity of 117 mV/(m/s)/mW with a high bandwidth of 60 kHz and a large flow range close to 26 m/s for the airflow. The high sensitivity and wide dynamic range achieved by our MEMS flow sensor enable its deployment as a promising sensing node for direct wall shear stress measurement applications.

Author Contributions: Conceptualization, J.N. and K.A.; methodology, J.N.; validation, J.N., S.M. and K.A.; formal analysis, J.N.; resources, S.M.; supervision, J.N.; project administration, J.N. All authors have read and agreed to the published version of the manuscript.

Funding: This research received no external funding.

Acknowledgments: This project was supported by the Deanship of Scientific Research at Prince Sattam Bin Abdulaziz University under the research project 2020/01/14293.

Conflicts of Interest: The authors declare no conflict of interest.

References

1. Löfdahl, L.; Gad-el-Hak, M. MEMS-based pressure and shear stress sensors for turbulent flows. *Meas. Sci. Technol.* **1999**, *10*, 66.
2. Chandrasekharan, V.; Sells, J.; Meloy, J.; Arnold, D.P.; Sheplak, M. A microscale differential capacitive direct wall-shear-stress sensor. *J. Microelectromechan. Syst.* **2011**, *20*, 622–635.
3. Chen, P.; Zhao, Y.; Li, Y. Fluid structure interaction analysis and simulation of micromachined cantilever-based flow sensor. In Proceedings of the 9th IEEE International Conference on Nano/Micro Engineered and Molecular Systems (NEMS), Waikiki Beach, HI, USA, 13–16 April 2014; pp. 350–353.
4. André, N.; Rue, B.; Scheen, G.; Flandre, D.; Francis, L.A.; Raskin, J.P. Out-of-plane MEMS-based mechanical airflow sensor co-integrated in SOI CMOS technology. *Sens. Actuators Phys.* **2014**, *206*, 67–74.
5. Von Papen, T.; Buder, U.; Ngo, H.D.; Obermeier, E. A second-generation MEMS surface fence sensor for high-resolution wall shear stress measurement. *Sens. Actuators Phys.* **2004**, *113*, 151–155.
6. Ioppolo, T.; Ayaz, U.K.; Otugen, M.V. Performance of a micro-optical wall shear stress sensor based on whispering gallery mode resonators. In Proceedings of the 47th AIAA Aerospace Sciences Meeting, Orlando, FL, USA, 5–8 January 2009.
7. Große, S.; Schröder, W. Dynamic wall-shear stress measurements in turbulent pipe flow using the micro-pillar sensor MPS3. *Int. J. Heat Fluid Flow* **2008**, *29*, 830–840.
8. Talbi, A.; Gimeno, L.; Gerbedoen, J.C.; Vard, R.; Soltani, A.; Mortet, V.; Preobeazhensky, V.; Merlen, A.; Pernod, P. A micro-scale hot wire anemometer based on low stress (Ni/W) multi-layers deposited on nanocrystalline diamond for airflow sensing. *J. Micromech. Microeng.* **2015**, *25*, 125029.
9. Xu, W.; Duan, M.; Ahmed, M.; Bermak, A.; Lee, Y.K. A three-dimensional integrated micro calorimetric flow sensor in CMOS MEMS technology. *IEEE Sens. Lett.* **2019**, *3*, 5500104.
10. Fan, Y.; Arwatz, G.; Van Buren, T.W.; Hoffman, D.E.; Hultmark, M. Nanoscale sensing devices for turbulence measurements. *Exp. Fluids* **2015**, *56*, 138.
11. Vereshchagina, E.; Tiggelaar, R.M.; Sanders, R.G.P.; Wolters, R.A.M.; Gardeniers, J.G.E. Low power micro-calorimetric sensors for analysis of gaseous samples. *Sens. Actuators B Chem.* **2015**, *206*, 772–787.
12. Zhu, Y.; Qin, M.; Huang, J.; Yi, Z.; Huang, Q.A. Sensitivity improvement of a 2D MEMS thermal wind sensor for low-Power applications. *IEEE Sens. J.* **2016**, *16*, 4300–4308.
13. Miao, J.J.; Leu, T.S.; Yu, J.M.; Tu, J.K.; Wang, C.T.; Lebiga, V.; Mironov, D.; Park, A.; Zinoviyeg, V.; Chung, K.M. MemS thermal film sensors for unsteady flow measurement. *Sens. Actuators Phys.* **2015**, *235*, 1–13.
14. Leu, T.S.; Yu, J.M.; Miao, J.J.; Chen, S.J. MEMS flexible thermal flow sensors for measurement of unsteady flow above a pitching wind turbine blade. *Exp. Therm. Fluid Sci.* **2016**, *77*, 167–178.
15. Shikida, M.; Yoshikawa, K.; Iwai, S.; Sato, K. Flexible flow sensor for large-scale air-conditioning network systems. *Sens. Actuators A Phys.* **2012**, *188*, 2–8.
16. Haneef, I.; Umer, M.; Mansoor, M.; Akhtar, S.; Rafiq, M.A.; Ali, S.Z.; Udreă, F. A tungsten based SOI CMOS MEMS wall shear stress sensor. *Sensors*, **2014**, IEEE, Valencia Spain, pp. 1475–1478.
17. Watmuff, A.H. An investigation of the constant-temperature hot-wire anemometer. *Exp. Therm. Fluid Sci.* **1995**, *11*, 117–134.
18. Freymuth, P. Feedback control theory for constant temperature hot-wire anemometers. *Rev. Sci. Instrum.* **1967**, *38*, 677–681.

19. Perry, A.E. *Hot-Wire Anemometry*; Oxford University Press: New York, NY, USA, 1982.
20. Makinwa, K.A.A.; Huijsing, J.H. A smart wind sensor using thermal sigma-delta modulation techniques. *Sens. Actuators* **2002**, *97*, 15–20.
21. Sosna, C.; Buchner, R.; Lang, W. A temperature compensation circuit for thermal flow sensors operated in constant-temperature-difference mode. *IEEE Trans. Instrum. Meas.* **2010**, *59*, 1715–1721.
22. Samie, M.; Watmuff, A.H.; Van Buren, T.; Hutchins, N.; Marusic, I.; Hultmark, M.; Smits, A.J. Modelling and operation of sub-miniature constant temperature hot-wire anemometry. *Meas. Sci. Technol.* **2016**, *27*, 125301.
23. Glatzl, T.; Steiner, H.; Kohl, F.; Sauter, T.; and Keplinger, F. Development of an air flow sensor for heating, ventilating, and air conditioning systems based on printed circuit board technology. *Sens. Actuators A Phys.* **2016**, *237*, 1–8.
24. Van Putten, A.; Middelhoek, S. Integrated silicon anemometer. *Electron. Lett.* **1974**, *10*, 425.
25. Wang, Y.H.; Chen, C.P.; Chang, C.M.; Lin, C.P.; Lin, C.H.; Fu, L.M.; Lee, C.Y. MEMS-based gas flow sensors. *Microfluid. Nanofluidics* **2009**, *6*, 333–346.
26. Kuo, J.T.W.; Yu, L.; Meng, E. Micromachined thermal flow sensors-A review. *Micromachines* **2012**, *3*, 550–573.
27. Gardner, E.L.; Vincent, T.A.; Jones, R.G.; Gardner, J.W.; Coull, J.; De Luca, A.; Udrea, F. MEMS thermal flow sensors an accuracy investigation. *IEEE Sens. J.* **2019**, *19*, 2991–2998.
28. Ye, Y.; Yi, Z.; Gao, S.; Qin, M.; Huang, Q.A. Octagon-shaped 2-D micromachined thermal wind sensor for high-accurate applications. *J. Microelectromech. Syst.* **2018**, *27*, 739–747.
29. Xue, D.; Zhou, W.; Ni, Z.; Wang, J.; Li, X. A front-side microfabricated tiny-size thermoresistive gas flow sensor with low cost, high sensitivity, and quick response. In Proceedings of the 2019 20th International Conference on Solid-State Sensors, Actuators and Microsystems & Eurosensors XXXIII (TRANSDUCERS & EUROSENSORS XXXIII), Berlin, Germany, 23–27 June 2019; pp. 1945–1948.
30. Baltes, H.; Paul, O.; Brand, O. Micromachined thermally based CMOS microsensors. *Proc. IEEE* **1998**, *86*, 1660–1678.
31. Qu, H. CMOS MEMS fabrication technologies and devices. *Micromachines* **2016**, *7*, 14.
32. Xu, W.; Ma, S.; Wang, X.; Chiu, Y.; Lee, Y.K. A CMOS-MEMS thermoresistive micro calorimetric flow sensor with temperature compensation. *J. Microelectromech. Syst.* **2019**, *28*, 841–849.
33. Shikida, M.; Yamazaki, Y.; Yoshikawa, K.; Sato, K. A MEMS flow sensor applied in a variable-air-volume unit in a building air-conditioning system. *Sens. Actuators A Phys.* **2013**, *189*, 212–217.
34. Freymuth, P. Frequency response and electronic testing for constant-temperature hot-wire anemometers. *J. Phys. E Sci. Instrum.* **1977**, *10*, 705–710.
35. Bruun, H.H. *Hot-Wire Anemometry: Principles and Signal Analysis*; Oxford University Press: Oxford, UK, 1995.
36. Mansoor, M.; Haneef, I.; Akhtar, S.; Rafiq, M.A.; De Luca, A.; Ali, S.Z.; Udrea, F. An SOI CMOS-based multi-sensor MEMS chip for fluidic applications. *Sensors* **2016**, *16*, 1608.
37. Ahmed, M.; Xu, W.; Mohamad, S.; Duan, M.; Lee, Y.K.; Bermak, A. Integrated CMOS-MEMS flow sensor with high sensitivity and large flow range. *IEEE Sens. J.* **2017**, *17*, 2318–2319.
38. Moser, D.; Baltes, H. A high sensitivity CMOS gas flow sensor on a thin dielectric membrane. *Sens. Actuators A Phys.* **1993**, *37–38*, 33–37.
39. Bruschi, P.; Dei, M.; Piotta, M. A single chip, double channel thermal flow meter. *Microsyst. Technol.* **2009**, *15*, 1179–1186.
40. Dong, Z.; Chen, J.; Qin, Y.; Qin, M.; Huang, Q.A. Fabrication of a micromachined two-dimensional wind sensor by Au–Au wafer bonding technology. *J. Microelectromech. Syst.* **2012**, *21*, 467–475.
41. Xu, W.; Wang, X.; Chiu, Y.; Lee, Y.K. High Sensitivity and Wide Dynamic Range Thermoresistive Micro Calorimetric Flow Sensor with CMOS MEMS Technology. *IEEE Sens. J.* **2020**, *20*, 4104–4111.

